Evolution of Global and Local Deformation in Additively Manufactured Octet Truss Lattice Structures

**Authors:** Elliott Jost \*, a, b, 1 David Moore b, 2, Christopher Saldana a, 3a George W. Woodruff School of Mechanical Engineering, Georgia Institute of Technology; 801 Ferst Drive, Atlanta, GA 30332, United States

Keywords: Additive manufacturing, computed tomography, lattice structure, octet truss

### 1 Abstract

Additively manufactured lattice truss structures, often referred to as architected cellular materials, present significant advantages over conventional structures due to their unique characteristics such as high strength-to-weight ratios and surface area-to-volume ratios. These geometrically complex structures, however, come with concomitant challenges for qualification and inspection. In this study, compression testing interrupted with microcomputed tomography inspection was conducted to monitor the evolution of global and local deformation throughout the loading process of 304L stainless steel octet truss lattice structures. Both two- and three-dimensional image analysis techniques were leveraged to characterize geometric heterogeneities resulting from the laser powder bed fusion manufacturing process as well as track the structure throughout deformation. Variations from model-predicted behavior resulting from these heterogeneities are considered relative to the predicted and actual responses of the structures during compression to better understand, model, and predict the octet truss lattice structure compression response.

#### 2 Introduction

Additively manufactured (AM) lattice truss structures, often referred to as architected cellular materials, present significant advantages over conventionally manufactured structures due to their high strength-to-weight ratios and tailorable properties [1–3]. This makes them of particular interest for aerospace applications, which often seek to minimize weight, and for medical applications for their tailorable properties and osteointegration capability [2,4]. Within the category of cellular structures, lattices are often favorable when compared to stochastic structures, more commonly known as foams, in large part because of the increased geometric control available for AM processes compared to foaming processes. However, AM surface textures are still far more complex than machined components [2]. Recent advances in metal additive manufacturing related to dimensional accuracy and repeatability have resulted in increased research interest in the use of lattice structures [5–8].

Despite the aforementioned advantages of lattice structures, there are concomitant challenges for modeling, qualification, and inspection [9–15]. Among these challenges are 1) structural fragility, 2) geometric complexity, 3) inspection procedures and the associated access requirements, 4) post-processing, and 5) common AM issues. With strut diameters often in the range of 200-800 µm, lattice structures can be easily damaged during manufacturing, handling, or post-processing procedures [16]. Additionally, the complexity of thousands of struts makes computer models and inspection data analysis algorithms relatively slow [17,18]. Lastly, common AM issues such as porosity [19–24], surface roughness [25–27], and structural heterogeneities persist as issues for lattices, and are often magnified in their effects due to their size scale [11,28,29].

<sup>&</sup>lt;sup>b</sup> Sandia National Laboratories; P.O. Box 5800, Albuquerque, NM 87185, United States

<sup>&</sup>lt;sup>1</sup> ejost@gatech.edu

<sup>&</sup>lt;sup>2</sup> dgmoore@sandia.gov

<sup>&</sup>lt;sup>3</sup> christopher.saldana@me.gatech.edu

<sup>\*</sup> Corresponding Author

While lattices have been studied for their global properties and nominal failure patterns, there has been relatively little work performed to study local failure patterns and how local defects influence macroscale deformation behavior. The intent of this study is to bring attention to and address this research gap. To do so, quantitative inspection was leveraged to better understand the structural defects common in AM lattices. Then, using interrupted compression testing, lattices were periodically scanned using computed tomography (CT) throughout the compression process, resulting in high-fidelity observational data of lattice deformation evolution at many stages throughout compression.

### 3 Method and Materials

### 3.1 Manufacture

Two 304L stainless steel lattice structures consisting of octet truss unit cells of 4.5 mm side length and 0.375 mm strut diameter arranged in a 9x9x9 pattern with 1.5 mm thick top/bottom plates were manufactured for the present study. Laser powder bed fusion (LPBF), a manufacturing technique that utilizes laser energy to selectively fuse metal powder in a layer-by-layer sequence, was used. The nominal design as well as build and compression directions are shown in Figure 1. Samples were manufactured using a Renishaw AM250 LPBF machine with the printing parameters for the bulk regions of 200 W laser power, exposure time of 75 μs, point distance of 60 μm, 85 μm hatch spacing, and respective border parameters of 150 W, 75 μs, and 20 μm. A 50 μm layer thickness was utilized. Lattices were oriented such that the plates were printed vertically. Gas-atomized powder from LPT Technology Ltd. was used with a nominal D<sub>10</sub>-D<sub>90</sub> diameter distribution of 15-45 μm. Samples were separated from the buildplate using a wire EDM without further post-processing.

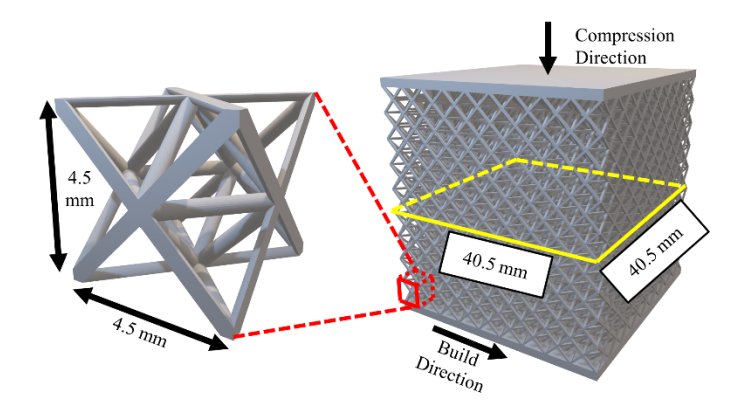


Figure 1. CAD model of the full lattice and the octet truss unit cell design. Build direction and compression direction annotated. Area used for global stress calculation denoted in yellow.

# 3.2 Computed Tomography Inspections

Samples were inspected using x-ray CT to image their complex structure in three dimensions for geometrical assessment. Scans were performed ex-situ in the printed state as well as at every deformation step using a Nikon Dual Head M2 225/450 kV CT machine and achieved a scan resolution of ~30 mm/voxel edge. A fixture was designed to allow for consistent alignment of the lattice bottom plate within the scanning volume. A tabular summary of CT inspection parameters is presented in

Table 1. Identical scan parameters were used for all scans conducted.

CT Parameter	Value
Acceleration Voltage	440 kV
Current	193 μΑ
Prefilter	2.4 mm Cu
Exposure time	500 ms
Projection Count	3141
Scan Time	56 min
Images Averaged Per Projection	2
Resolution/Voxel Side Length	30.2 μm

# 3.3 Characterization Techniques

Many features of printed lattice structures are of interest for characterization due to their deviation from nominal geometries. Geometric lattice defects can be classified into three broad categories: dimensional inaccuracies, surface texture, and porosity [2]. The present paper focuses primarily on dimensional inaccuracies, which are of particular significance in lattices, where they can be on the size scale of the struts of the lattice. This can result in significant local structural performance variations that can alter global performance, as will be shown in the ensuing.

First, scans were reconstructed using a filtered back projection algorithm in Nikon Metrology's CT Pro software. Then, the commercial CT data analysis software Volume Graphics VGSTUDIO MAX 3.4 (VG) was used to determine a surface. Using a best fit registration function, the CT data was registered to the coordinate system of the nominal CAD geometry.

To assess strut geometric accuracy of the printed state, a MATLAB script was developed. The analysis included strut cross-section assessment, wherein modelling the strut cross section of all lattice struts as ellipses was conducted. This analysis provided an assessment of the overall lattice structure geometry by modelling approximately 1.1 million ellipses per sample, providing a large sampling of strut cross-section data. While other studies have conducted similar strut assessment procedures by fitting circles to strut cross-sections [30,31], the present study, as well as Ref. [32], utilized ellipses due to the high observed cross-section eccentricity, increasing the representational accuracy of the analysis.

The ellipse-based strut geometry assessment was conducted as follows. First, the scanned CT volume is registered to the CAD model and interpolated image slices of the volume in the newly-defined voxel grid were extracted from the six planes perpendicular to the strut cylinders (Figure 2a). These lattice-level images were imported as into MATLAB and binarized using a grayscale threshold informed by the more complex Volume Graphics surface determination. Gridded windows were then created around each strut location and strut-level image stacks for each perpendicular strut area created (Figure 2b). Next, a strut cross-section of interest was identified, the boundary was determined, and an ellipse was fit to the cross-section using a least squares framework (Figure 2c). From the fitted ellipses, many parameters of interest could be extracted to characterize the struts, including ellipse major and minor axis length, the ratio of these two, and strut waviness, defined as offset of the ellipse center from mean strut center. This analysis provided for the ability to characterize printed struts at different build orientations. Nomenclature for these strut types is provided in Table 2.

Porosity analyses were performed using the VG software and it was found that parts were near fully-dense with very few pores identified at the CT resolution used. As such, internal defects were not considered in analysis of these structures due to a limited anticipated impact on performance.

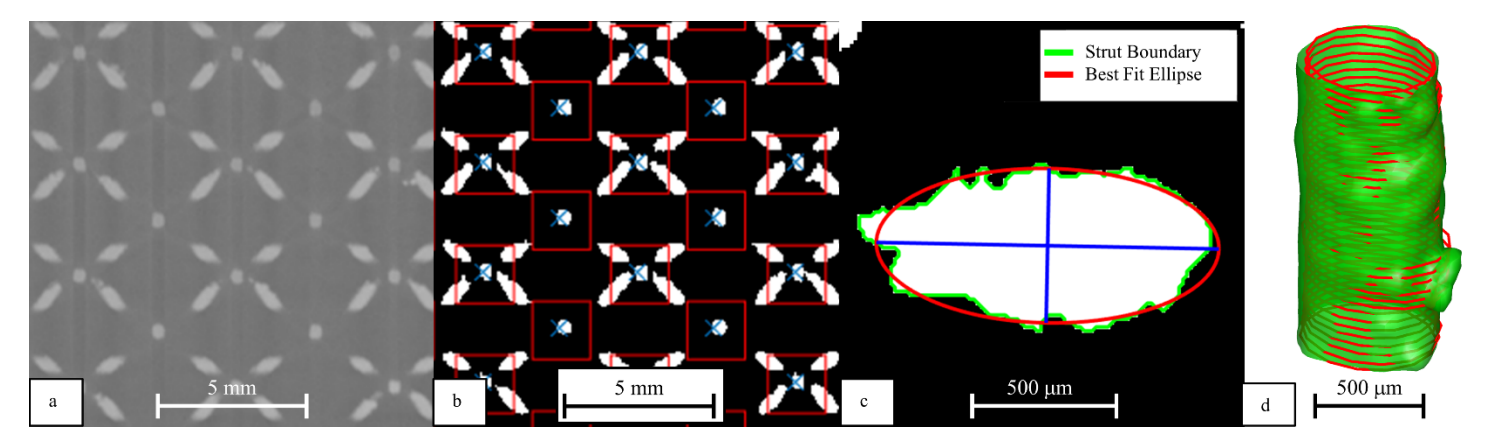


Figure 2. Strut ellipse-fitting process. a) Grayscale CT image slice imported. b) Image binarized and strut locations identified. c) Strut boundary identified (green), ellipse fitted (red), and axes identified (blue). d) Red best fit ellipses characterizing an individual strut shown as semi-transparent.

Table 2. Strut type definitions. Figure and print coordinate system (CS) provided to show direction of strut types. Samples were built in the +Z, [0, 0, 1] direction and loaded along the Y-axis, [0, 1, 0] direction.

/ L / /	3	0	/ L / / J
Strut	Direction	r	_
Type	(Print CS)	3	4
1	[0, 1, 1]	Y	
2	[0, 1, -1]	X	6
3	[1, 0, 1]	Z	
4	[1, 0, -1]		2 5
5	[1, 1, 0]	40.5 mm	
6	[1, -1, 0]	$\circ m_{m}$	

### 3.4 Mechanical Testing

Mechanical compression testing was performed using a servo-hydraulic MTS load frame equipped with an 88-kN load cell. A friction-free boundary condition was simulated by applying a thin layer of oil-based lubricant to the lattice plates. This step is important, as this boundary condition has a significant effect on failure behavior, as seen when comparing the results of models developed in Refs [30,33][33]. Samples were loaded in displacement control at a rate of 0.0127 mm/s ( $2.9 \times 10^{-4} \text{ mm/mm/s}$ ), meeting the quasi-static testing criterion of ASTM E9-09 [34]. Once a sample had been displaced ~5-10 millistrain, the sample was unloaded, removed from the load stage, and CT scanned in its deformed state. Global strain values, denoted  $\varepsilon_g$ , are reported as the highest global strain value experienced by the lattices and are calculated using the height of the lattice as measured using the testing stage displacement divided by the original height of the lattice, including the printed plates. The innate stage compliance was accounted for in all strain calculations. Additionally, it should be noted that reported stress values are global stress values calculated using the bounding lattice area of 40.5 x 40.5 mm shown in Figure 1.

#### 4 Results

#### 4.1 Characterization

The above characterization methodology was applied and the results presented below are organized by characterization technique. These characterizations serve to highlight the significance of the dimensional inaccuracies observed in lattices.

Figure 3 shows the major and minor axis length distribution information gathered from this analysis as histograms as well as overlaid normal distributions for Sample 1. As can be seen in this figure, both the major and minor axis lengths are well-modelled by Gaussian normal distributions for all strut types, despite significant differences in the mean value and standard deviation. Mean values for diagonally printed struts (types 1-4) were in the 380-470  $\mu$ m range, approximately 0-25% oversized when compared to the nominal strut diameter of 375  $\mu$ m. However, horizontally printed struts (types 5 and 6) exhibit significantly larger major axis length than the other strut types, with the mean value occurring at 580-610  $\mu$ m, or ~55-60% oversized. The observed print orientation-dependence of the strut major axis length is due to the overhangs and extraneous material on horizontal struts. Overhang defects and overprinting associated with horizontal parts, especially lattice struts, is a phenomena which has been observed elsewhere. These defects can serve to create stress concentrators and play a significant role in apparent mechanical properties at the sub-millimeter scale, resulting in stresses as high as an order of magnitude above the nominal stress [11].

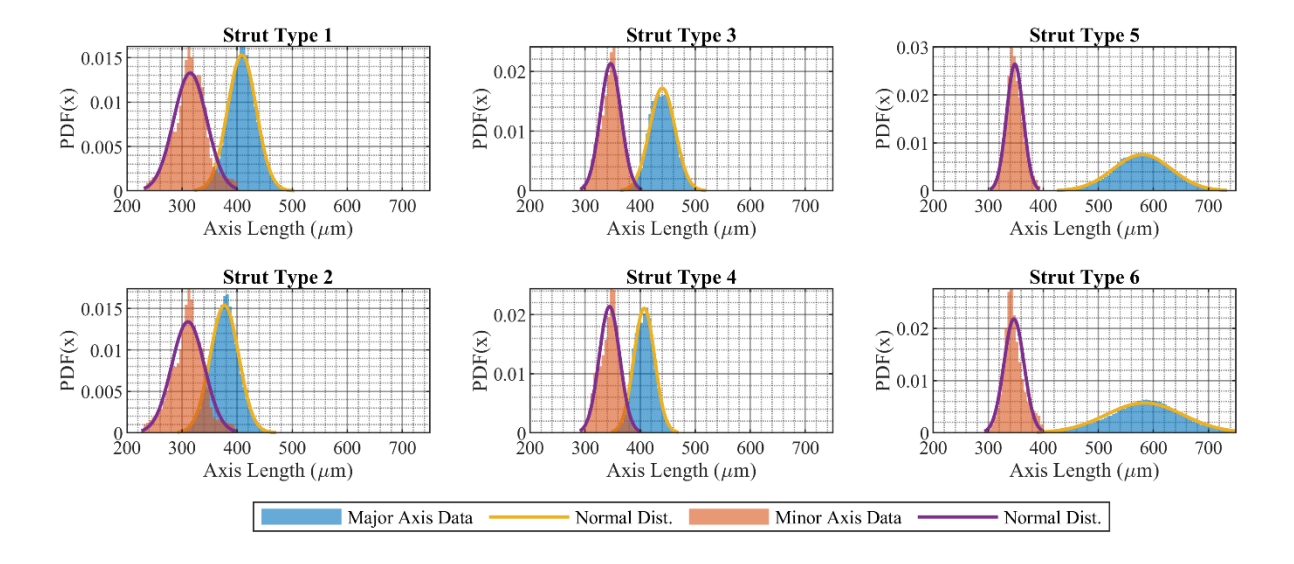


Figure 3. Major and minor axis lengths of Sample 1 as calculated by the strut ellipse fitting algorithm. Strut type definitions provided in Table 2.

It is well established that horizontal struts in lattices of this strut size commonly have defects that can significantly impact the mechanical behavior of the struts as a result [11]. Because major axis length of the horizontally printed struts was significantly larger than the nominal strut dimension, it is anticipated that the lattices may exhibit a consequential deviation from its nominal orthotropy [35], although this has not been quantified in the present study. Furthermore, the horizontal struts in the octet truss lattice, which are loaded in tension when the global loading is compression [33], have been shown to exhibit behavior dominated by surface roughness and heterogeneities [11,29].

Beyond size, strut shape can play a significant role in lattice performance due to the changes in area moment of inertia. This affects bending moments at the strut level, which is particularly critical to failure behavior, and

particularly so in lattices of ductile metals, which exhibit significant plasticity. As will be shown in the ensuing, bending of struts is the primary mechanism by which failure initiates. Thus, the ratio of the minor and major axis lengths, a measurement of the cross-sectional eccentricity, is useful in understanding lattice quality and performance. An ellipse with an axis ratio of 1.0 would be perfectly circular whereas an ellipse with an axis ratio of 0.5 would be highly eccentric, with the major axis being twice as long as the minor axis.

Figure 4 presents this data, as well as a summary of the axis length information in boxplot form. As shown in this figure, diagonally printed struts (types 1-4) had much higher axis ratios in the range of 0.75-0.85 than the horizontally printed struts (types 5 and 6) at  $\sim$ 0.60. This indicates that not only were the horizontally-printed struts oversized but also that these struts were highly eccentric and non-cylindrical. Ellipse orientation information indicated that elliptical cross sections for horizontal struts were such that their major axis was parallel to the z-direction in the printer.

Lastly, Figure 4 presents strut waviness, measured as the offset from the ideal strut axis. This data shows that the diagonal struts exhibit relatively constant cross-sectional offset, whereas horizontally-printed struts tend to have more significant deviation from nominal. Modeling efforts such as in Ref. [36] have shown strut waviness to play a significant role in dictating lattice performance. Strut waviness variation further emphasizes the significant heterogeneous geometry characteristic of LPBF lattices.

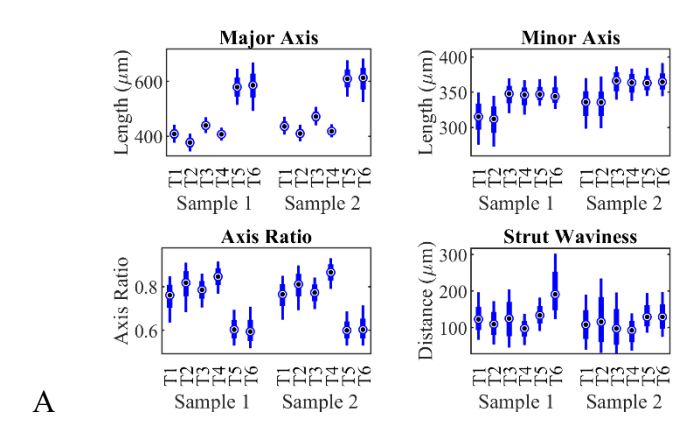


Figure 4. Boxplots of Major and Minor Axis Length, Axis Ratio, and Strut Waviness. The central mark indicates the median, the box extents indicate the 25<sup>th</sup> and 75<sup>th</sup> percentiles and the whisker extents indicate the 10<sup>th</sup> and 90<sup>th</sup> percentiles.

# 4.2 Mechanical Compression Testing

The stress-strain response from mechanical compression testing is shown in Figure 5. These results show the individual compression tests combined to form the "global" stress-strain curve of the lattice structures. For each compression test, an initial elastic deformation of 0.0075 mm/mm is seen, followed by movement along what forms the global compression curve. Finally, an elastic recovery of 0.0075 mm/mm can be seen for each test. Globally, the first maximum compressive stress of the lattice can be seen at ~0.03 mm/mm strain, followed by a force relaxation as the initial lattice cell layer plastically collapses.

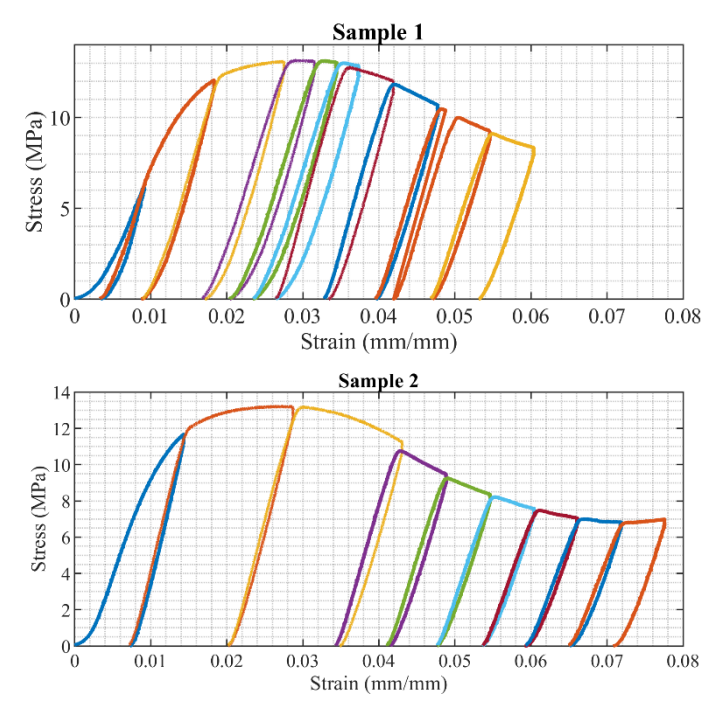


Figure 5. Mechanical testing results from Sample 1 and Sample 2.

# 4.3 Deformation Evolution

Using CT inspection data obtained at different global strain, the failure behavior and deformation evolution of the lattices was tracked and analyzed. The following section is separated into global failure behavior, which focuses on the broad failure pattern of the lattices, and local failure behavior, which focuses on the strut-level behavior that initiated the global failure process and, as will be shown, determines the global failure.

#### 4.3.1 Global Failure Behavior

The global failure behavior of the lattices can be observed by comparing progressive CT scan data from various global strain values. Below, Figure 6 presents deformed lattices annotated with red lines to highlight the approximate failure boundary on each lattice face. As Figure 6 shows, the collapse or failure surface was not a perfect plane as predicted by FE modelling based on perfect CAD geometry [30] which predicts a failure plane with a normal in the [1, 1, 1] direction. Instead, this figure shows that the failure surface appears to be highly complex, at least as viewed from the lattice surface.

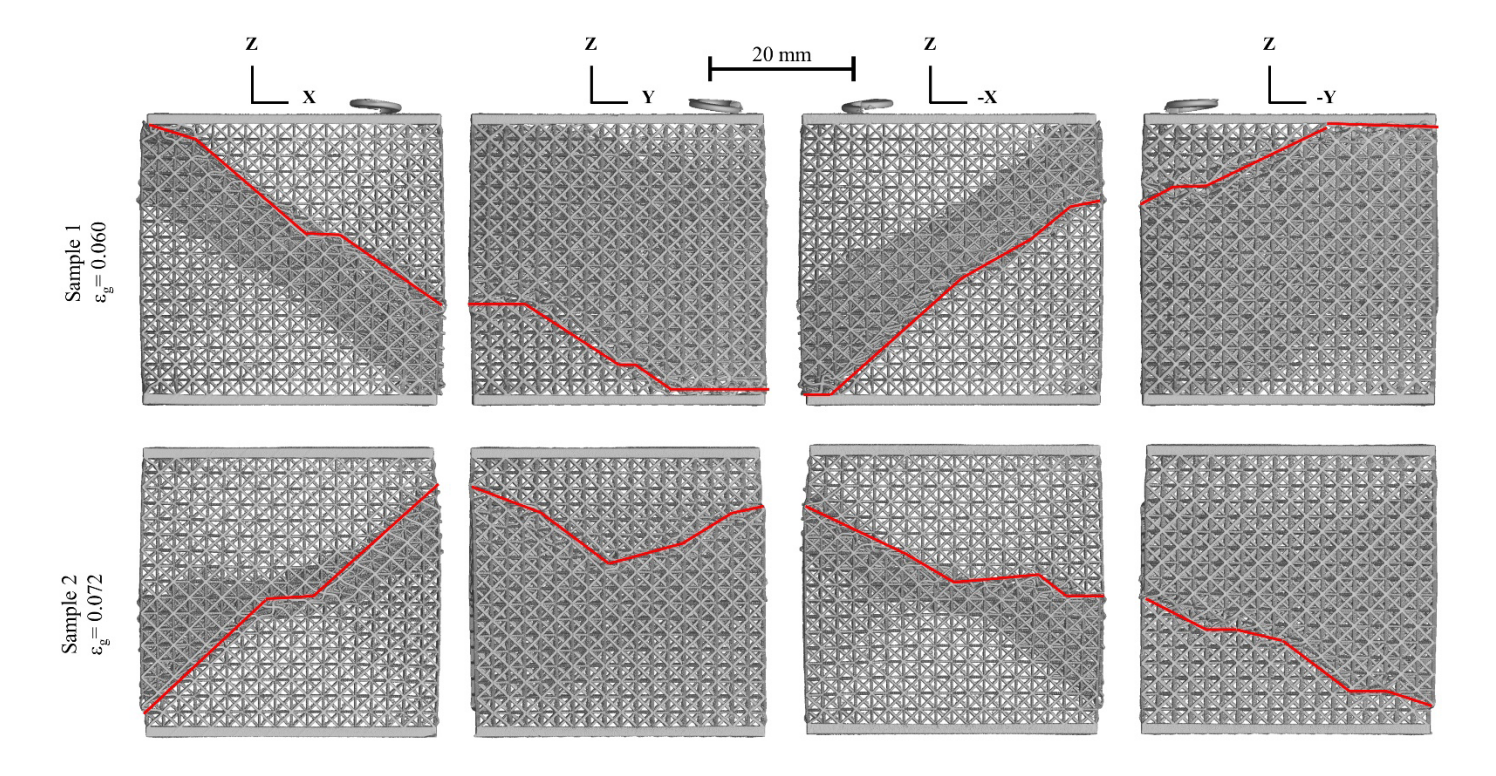


Figure 6. CT scans of Samples 1 and 2 and large global strains. Red lines drawn to indicate the approximate failure surface on each face of the lattices.

To further study the global failure beyond the lattice's surface, an image processing script was developed to identify the complex failure surface in three dimensions. By identifying the failed cells in 2D slices in the XZ plane and separating the regions above and below this identified surface, a three-dimensional failure surface estimate was created by linearly interpolating the identified points. The resulting failure surface and separated regions of Sample 2 at 7.2% global strain are shown in Figure 7. As seen in this figure, the actual failure is not a simple plane, but is instead a complex, tortuous surface. The complex texture of this surface reflects the stress variations present in the lattice struts, a concept which will be further elucidated in the ensuing discussion.

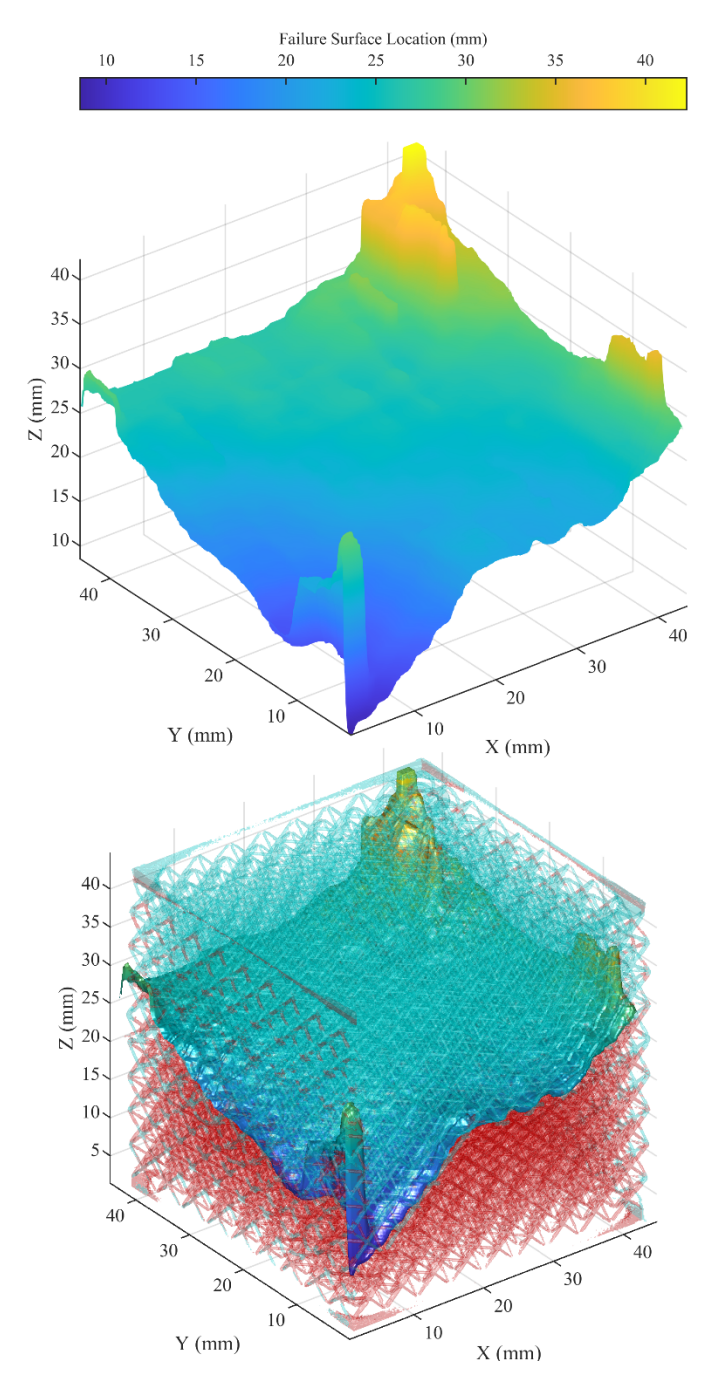


Figure 7. Sample 2 a) failure surface and b) semi-transparent lattice volume divided above and below failure. CT scan of lattice at 7.2% global strain used for this analysis. Lattice regions above and below the failure are shown in teal and red, respectively.

### 4.3.2 Local Failure Behavior

In addition to global failure behavior, the relatively high scanning resolution of the CT data gathered offers a look at the initiation of failure at the unit cell and even single strut level. Figure 8 shows a view of the failure-initiating strut in Sample 1 and the subsequent development of a shear band, the defining global failure pattern as seen above in Figure 6 and Figure 7. As can be seen in Figure 8a-d, failure initiated at the struts located in the top corner of the lattice, highlighted in Figure 8a with a red box. A closer view is shown in Figure 8e-h of the failure-initiating struts, labelled  $\alpha$  in Figure 8e, at the same strain levels. This figure clearly shows that the strut began

failing by elastically deforming (Figure 8a and Figure 8e) at 0.9% global strain followed by bending in Figure 8b and Figure 8f seen at 3.2% strain. Once this strut began to plastically deform, failure propagated to struts labelled as  $\beta$  in the surrounding region, which began to fail in plastic bending, seen in Figure 8d at 4.2% strain, until a clearly defined failure band emerged in Figure 8 data strain of 6.0%. The creation of plastic hinges, the evolution of which is shown most clearly in the figure at strain values of 3.2% and 4.2%, corresponded to just before and just after the maximum compressive stress seen in the stress-strain curves of Figure 5.

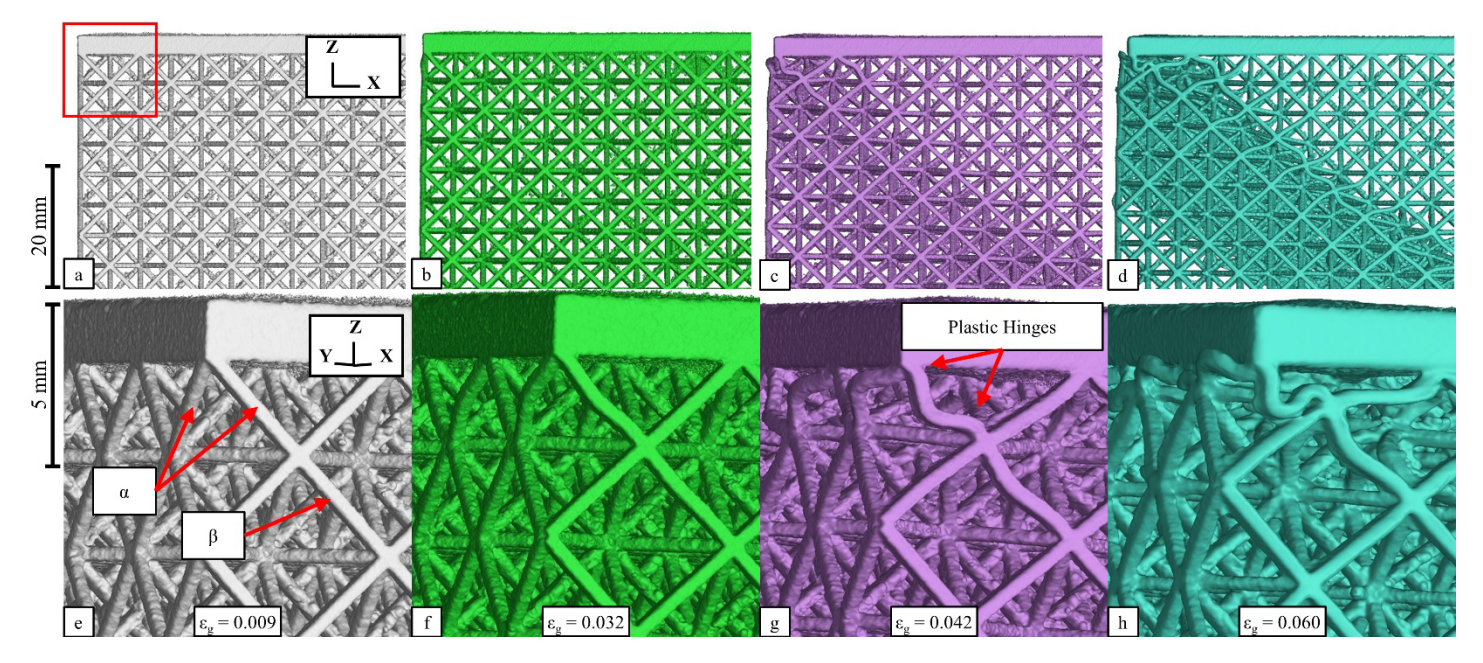


Figure 8. CT scans of Sample 1 throughout the failure process showing the deformation evolution of the failure-initiating area (a-d) and the failure-initiating strut (e-h). Region shown in subfigures e-h highlighted in subfigure a.

### 5 Discussion

Results from compression testing interrupted with CT inspections presented in the above figures serve to provide insight into the failure mechanisms and behavior, both global and local, that occur during 304L octet truss lattice compression. These figures present intuitive three-dimensional imaging of the lattice at various stages of deformation typically only seen in finite element simulations.

# 5.1 Global Failure Behavior

The global failure behavior shown in Figure 6 and Figure 7 as a distorted shear band highlights the effects of structural heterogeneities on failure behavior. These figures present a broad pattern of shear band failure but, upon closer inspection, reveal significant deviations from the planar shear band surface predicted by FE simulation of perfect lattice geometries, such as those presented in Refs. [30,37].

The failure surfaces observed in the present study more closely resemble an intergranular fracture path of a polycrystalline material following the path of least resistance [38] rather than a neat, mathematically planar shear failure. In an intergranular fracture the path is dictated by the grain boundaries, which are relatively weak compared to the surrounding areas, and in the lattice case by local geometry variations that result in struts that are relatively weak compared to the surrounding struts. As described in Ref. [30], variations between the horizontal and diagonal strut diameters can lead to a transition from a near perfect angled shear band to a complete horizontal failure. In addition, Ref. [37] describes how nodal stiffening mechanisms can influence and ultimately change the failure mode from a shear band-style failure pattern to one of horizontal layer-by-layer collapse. These prior

works demonstrate the influence of small geometric changes on global failure behavior. In the present work, geometric defects characterized above such as cross-sectional size variation, eccentricity, strut waviness and build orientation dependency were observed to have led to a failure mode between these two extremes.

It is possible that the significant structural heterogeneities presented and quantified through the ellipse-based strut geometry assessment contributed to the tortuous failure surfaces identified and shown in Figure 6 and Figure 7. In this case, the structural heterogeneities effectively created struts whose mechanical properties were non-uniform with respect to one another. A similar hypothesis is presented by prior studies who have observed deviations from expected behavior [39]. Structural imperfections of this kind, common to small-scale AM powder bed printing, have been shown to serve as stress concentrations resulting in local stresses in excess of an order of magnitude above the nominal, bulk stress state [11]. These structural imperfections, which result in non-uniform, off-nominal stresses in the strut, can create wide ranges of effective structural properties for each strut [40,41]. It is hypothesized that the significant stress deviations from nominal stress levels resulting from structural heterogeneities influenced the failure surface. In essence, these defects and print imperfections determine, at least in part, the path of least resistance for the failure surface by altering the individual geometry and therefore structural performance of each strut. It is hypothesized that the arrangement of strut geometries and the resulting effective properties influenced the precise failure behavior observed in the present results.

# 5.2 Local Failure Behavior

In addition to global failure behavior, local failure mechanisms at the strut-level were identified and observed in this study and can be compared to behavior described by cellular structure theory. As presented in Figure 8, the global plastic collapse of the lattice initiated at two low-connectivity struts in an individual unit cell in the corner of Sample 1, consistent with traditional cellular structure theory, which, by the Maxwell criterion for static determinacy [35], dictates that nodes with lesser connectivity are able to sustain less stress in compression than those with higher levels of connectivity. In the context of octet truss lattices, unit cell corner nodes within the bulk of the structure have a connectivity of 12 compared to those at the corner of lattice structures, which only have a connectivity of 3, with two of the connecting struts being only a quarter of a cylinder. This difference in connectivity is one reason why failure occurred at the corner node shown in Figure 8. Based on the observed initiation of global failure at corner nodes, it is probable that significant improvements in lattice maximum compressive stress can be achieved with very marginal weight gain by reinforcing the top and bottom corner node of the lattice or, alternatively, all nodes at lattice corners at each z-level. Such a modified lattice design would be similar to the vertical struts added to the FCC unit cell to create the FCCZ unit cell. Similar designs have been implemented at the unit cell level and have been shown to actuate significant improvements in lattice stiffness and strength properties [42,43].

Beyond the fact that failure initiated at a lattice corner node, the CT scans of the failure-initiating strut beginning to fail provide direct evidence of strut-level plastic collapse and the creation of plastic hinges. The failure-initiating struts were subject to bending moments which exceeded a critical threshold, resulting in severe plastic deformation. As described in Ref. [44], when the bending moment of a strut becomes greater than its plastic moment, determined as a function of material properties and geometry, plastic collapse begins and a plastic hinge is formed. Beyond the α struts of Figure 8e, similar plastic hinging behavior can be seen throughout the failure surface partially shown in Figure 8d. The bending moment can be directly related to the area moment of inertia dictated by the shape of the cross section as well as the cross-section offset defined here as strut waviness. As the ellipse-based strut assessment results show, strut cross sections can vary widely in size. As a result of this cross-sectional variation, the plastic moment that is required to be overcome to initiate plastic collapse can vary widely from strut to strut. Furthermore, the significant strut waviness can result in eccentric, off-center loading, making struts with higher strut waviness collapse under buckling at below-nominal loads. Overall, inter- and intra-strut geometry variations, such as those observed in Figure 3 and Figure 4, may influence the precise global failure surface by creating a path of least resistance as the lattice structures failed under compressive loading.

#### 6 Conclusion

Using compression testing interrupted with CT scans this study presented three-dimensional imaging revealing the evolution of deformation in octet truss lattices made from 304L stainless steel. Initiation of deformation was observed to occur at corner nodes, likely due to their low connectivity to the rest of the structure compared to internal nodes. The interrupted testing method allowed not only for the monitoring of failure mechanisms and location of deformation initiation, but provided data that can be directly compared to failure and deformation modes predicted by finite element models.

In addition, various CT data characterization tools were leveraged to thoroughly characterize lattice strut deviation. Statistical characterization revealed significant deviations from nominal geometry in all strut types, and especially in horizontally printed struts, suggesting that loading direction of lattices is an important design consideration, even when bulk lattice behavior is nominally orthotropic. Characterizations performed confirmed previously reported results showing that horizontal struts often exhibit worse geometric accuracy.

Furthermore, the CT imaging results provided for direct observation of mechanisms of deformation described by cellular structure theory, namely the development of plastic hinges and its progression throughout a lattice as plastic collapse occurs. Lastly, it was seen that the failure surface for initial plastic collapse in real lattices is complex and influenced by local mechanical properties of individual struts as dictated by their actual printed geometry, suggesting the need for the incorporation of realistic manufacturing defects in models attempting to simulate the failure of AM metallic lattices.

# 7 CRediT authorship contribution statement

**Elliott W. Jost:** Conceptualization, Data curation, Investigation, Formal analysis, Methodology, Software, Writing – original draft, Writing – review & editing. **David G. Moore:** Resources, Supervision, Funding acquisition. **Christopher Saldana:** Resources, Supervision, Funding acquisition, Writing – review & editing.

# 8 Declaration of Competing Interest

The authors declare that they have no known competing financial interests or personal relationships that could have appeared to influence the work reported in this paper.

# 9 Acknowledgement

The authors would like to acknowledge and thank Ben Brown at the Kansas City National Security Campus for the manufacture of the samples used in this study. Additionally, the authors would like to thank Jaime Berez for his valuable feedback and useful conversations regarding this work.

This work was partially supported by NSF CMMI-1646013, CMMI-1825640 and IIP-1631803. This work was also supported by a fellowship from the American Society for Nondestructive Testing (ASNT) to EJ. Sandia National Laboratories is a multimission laboratory managed and operated by National Technology & Engineering Solutions of Sandia, LLC, a wholly owned subsidiary of Honeywell International Inc., for the U.S. Department of Energy's National Nuclear Security Administration under contract DE-NA0003525. This paper describes objective technical results and analysis. Any subjective views or opinions that might be expressed in the paper do not necessarily represent the views of the U.S. Department of Energy or the United States Government.

### 10 References

- [1] T.D. Ngo, Additive Manufacturing (3D Printing): A Review of Materials, Methods, Applications and Challenges, Composites Part B. (2018) 25.
- [2] I. Echeta, X. Feng, B. Dutton, R. Leach, S. Piano, Review of Defects in Lattice Structures Manufactured by Powder Bed Fusion, The International Journal of Advanced Manufacturing Technology. 106 (2020) 2649–2668. https://doi.org/10.1007/s00170-019-04753-4.
- [3] S. Xu, J. Shen, S. Zhou, X. Huang, Y.M. Xie, Design of Lattice Structures with Controlled Anisotropy, Materials and Design. (2016) 5.
- [4] J. Kadkhodapour, H. Montazerian, A.Ch. Darabi, A.P. Anaraki, S.M. Ahmadi, A.A. Zadpoor, S. Schmauder, Failure Mechanisms of Additively Manufactured Porous Biomaterials: Effects of Porosity and Type of Unit Cell, Journal of the Mechanical Behavior of Biomedical Materials. 50 (2015) 180–191. https://doi.org/10.1016/j.jmbbm.2015.06.012.
- [5] M. Benedetti, A. du Plessis, R.O. Ritchie, M. Dallago, S.M.J. Razavi, F. Berto, Architected cellular materials: A review on their mechanical properties towards fatigue-tolerant design and fabrication, Materials Science and Engineering: R: Reports. 144 (2021) 100606. https://doi.org/10.1016/j.mser.2021.100606.
- [6] E. Uribe-Lam, C.D. Treviño-Quintanilla, E. Cuan-Urquizo, O. Olvera-Silva, Use of additive manufacturing for the fabrication of cellular and lattice materials: a review, Null. 36 (2021) 257–280. https://doi.org/10.1080/10426914.2020.1819544.
- [7] G. Dong, Y. Tang, Y.F. Zhao, A Survey of Modeling of Lattice Structures Fabricated by Additive Manufacturing, Journal of Mechanical Design. 139 (2017) 100906. https://doi.org/10.1115/1.4037305.
- [8] C. Li, H. Lei, Z. Zhang, X. Zhang, H. Zhou, P. Wang, D. Fang, Architecture design of periodic truss-lattice cells for additive manufacturing, Additive Manufacturing. 34 (2020) 101172. https://doi.org/10.1016/j.addma.2020.101172.
- [9] A.P. Garland, B.C. White, B.H. Jared, M. Heiden, E. Donahue, B.L. Boyce, Deep Convolutional Neural Networks as a Rapid Screening Tool for Complex Additively Manufactured Structures, Additive Manufacturing, 35 (2020) 101217. https://doi.org/10.1016/j.addma.2020.101217.
- [10] M. Praniewicz, G. Ameta, J. Fox, C. Saldana, Data registration for multi-method qualification of additive manufactured components, Additive Manufacturing. 35 (2020) 101292. https://doi.org/10.1016/j.addma.2020.101292.
- [11] A.D. Dressler, E.W. Jost, J.C. Miers, D.G. Moore, C.C. Seepersad, B.L. Boyce, Heterogeneities dominate mechanical performance of additively manufactured metal lattice struts, Additive Manufacturing. 28 (2019) 692–703. https://doi.org/10.1016/j.addma.2019.06.011.
- [12] M. Smith, Z. Guan, W.J. Cantwell, Finite element modelling of the compressive response of lattice structures manufactured using the selective laser melting technique, International Journal of Mechanical Sciences. 67 (2013) 28–41. https://doi.org/10.1016/j.ijmecsci.2012.12.004.
- [13] Y. Amani, S. Dancette, P. Delroisse, A. Simar, E. Maire, Compression Behavior of Lattice Structures Produced by Selective Laser Melting: X-Ray Tomography Based Experimental and Finite Element Approaches, Acta Materialia. 159 (2018) 395–407. https://doi.org/10.1016/j.actamat.2018.08.030.
- [14] P. Sperling, A.D. Plessis, G. Schwaderer, Challenges and Approaches for Metrology of Additive Manufactured Lattice Structures by Industrial X-Ray Computed Tomography, (2020). https://doi.org/10.13140/RG.2.2.22433.12649.
- [15] M. Praniewicz, J. Fox, G. Ameta, F. Kim, P. Witherell, C. Saldana, Exploring Registration of Optical, CMM and XCT for Verification of Supplemental Surfaces to Define AM Lattices: Application to Cylindrical and Spherical Surfaces, Procedia CIRP. 92 (2020) 181–186. https://doi.org/10.1016/j.procir.2020.05.182.

- [16] E. Maleki, S. Bagherifard, M. Bandini, M. Guagliano, Surface post-treatments for metal additive manufacturing: Progress, challenges, and opportunities, Additive Manufacturing. (2020) 101619. https://doi.org/10.1016/j.addma.2020.101619.
- [17] B. Lozanovski, D. Downing, R. Tino, A. du Plessis, P. Tran, J. Jakeman, D. Shidid, C. Emmelmann, M. Qian, P. Choong, M. Brandt, M. Leary, Non-destructive simulation of node defects in additively manufactured lattice structures, Additive Manufacturing. 36 (2020) 101593. https://doi.org/10.1016/j.addma.2020.101593.
- [18] B. Lozanovski, D. Downing, P. Tran, D. Shidid, M. Qian, P. Choong, M. Brandt, M. Leary, A Monte Carlo simulation-based approach to realistic modelling of additively manufactured lattice structures, Additive Manufacturing. 32 (2020) 101092. https://doi.org/10.1016/j.addma.2020.101092.
- [19] A. du Plessis, I. Yadroitsava, I. Yadroitsev, Effects of Defects on Mechanical Properties in Metal Additive Manufacturing: A Review Focusing on X-Ray Tomography Insights, Materials & Design. 187 (2020) 108385. https://doi.org/10.1016/j.matdes.2019.108385.
- [20] G.M. Gladysz, K.K. Chawla, Chapter 2 Intrinsic Voids, Ideal Materials, and Real Materials, in: G.M. Gladysz, K.K. Chawla (Eds.), Voids in Materials, Elsevier, Amsterdam, 2015: pp. 13–35. https://doi.org/10.1016/B978-0-444-56367-5.00002-6.
- [21] F.H. Kim, S.P. Moylan, Literature Review of Metal Additive Manufacturing Defects, National Institute of Standards and Technology, Gaithersburg, MD, 2018. https://doi.org/10.6028/NIST.AMS.100-16.
- [22] F.H. Kim, S.P. Moylan, T.Q. Phan, E.J. Garboczi, Investigation of the Effect of Artificial Internal Defects on the Tensile Behavior of Laser Powder Bed Fusion 17–4 Stainless Steel Samples: Simultaneous Tensile Testing and X-Ray Computed Tomography, Experimental Mechanics. (2020). https://doi.org/10.1007/s11340-020-00604-6.
- [23] H. Masuo, Y. Tanaka, S. Morokoshi, H. Yagura, T. Uchida, Y. Yamamoto, Y. Murakami, Influence of Defects, Surface Roughness and Hip on the Fatigue Strength of Ti-6Al-4V Manufactured by Additive Manufacturing, International Journal of Fatigue. 117 (2018) 163–179. https://doi.org/10.1016/j.ijfatigue.2018.07.020.
- [24] S. Tammas-Williams, The Influence of Porosity on Fatigue Crack Initiation in Additively Manufactured Titanium Components, Scientific ReportS. (n.d.) 13.
- [25] V. Aloisi, S. Carmignato, Influence of Surface Roughness on X-Ray Computed Tomography Dimensional Measurements of Additive Manufactured Parts, Case Studies in Nondestructive Testing and Evaluation. 6 (2016) 104–110. https://doi.org/10.1016/j.csndt.2016.05.005.
- [26] H. Hassanin, A. Elshaer, R. Benhadj-Djilali, F. Modica, I. Fassi, Surface Finish Improvement of Additive Manufactured Metal Parts, in: K. Gupta (Ed.), Micro and Precision Manufacturing, Springer International Publishing, Cham, 2018: pp. 145–164. https://doi.org/10.1007/978-3-319-68801-5\_7.
- [27] P. Jiang, M. Rifat, S. Basu, Impact of Surface Roughness and Porosity on Lattice Structures Fabricated by Additive Manufacturing A Computational Study, in: Procedia Manufacturing, 2020: p. 9.
- [28] P.G. Coelho, L.D. Amiano, J.M. Guedes, H.C. Rodrigues, Scale-size effects analysis of optimal periodic material microstructures designed by the inverse homogenization method, Computers & Structures. 174 (2016) 21–32. https://doi.org/10.1016/j.compstruc.2015.10.001.
- [29] G. Meyer, F. Brenne, T. Niendorf, C. Mittelstedt, Influence of the Miniaturisation Effect on the Effective Stiffness of Lattice Structures in Additive Manufacturing, Metals. 10 (2020) 1442. https://doi.org/10.3390/met10111442.
- [30] L. Liu, P. Kamm, F. García-Moreno, J. Banhart, D. Pasini, Elastic and Failure Response of Imperfect Three-Dimensional Metallic Lattices: The Role of Geometric Defects Induced by Selective Laser Melting, Journal of the Mechanics and Physics of Solids. 107 (2017) 160–184. https://doi.org/10.1016/j.jmps.2017.07.003.
- [31] Z. Dong, Y. Liu, W. Li, J. Liang, Orientation dependency for microstructure, geometric accuracy and mechanical properties of selective laser melting AlSi10Mg lattices, Journal of Alloys and Compounds. 791 (2019) 490–500. https://doi.org/10.1016/j.jallcom.2019.03.344.

- [32] M. Dallago, F. Zanini, S. Carmignato, D. Pasini, M. Benedetti, Effect of the geometrical defectiveness on the mechanical properties of SLM biomedical Ti6Al4V lattices, Procedia Structural Integrity. 13 (2018) 161–167. https://doi.org/10.1016/j.prostr.2018.12.027.
- [33] B.B. Babamiri, Deformation Mechanisms and Post-Yielding Behavior of Additively Manufactured Lattice Structures, Materials and Design. (2020) 18.
- [34] E28 Committee, Test Methods for Tension Testing of Metallic Materials, ASTM International, n.d. https://doi.org/10.1520/E0008\_E0008M-11.
- [35] V.S. Deshpande, N.A. Fleck, M.F. Ashby, Effective Properties of the Octet-Truss Lattice Material, J. Mech. Phys. Solids. (2001) 23.
- [36] M. Dallago, On the Effect of Geometrical Imperfections and Defects on the Fatigue Strength of Cellular Lattice Structures Additively Manufactured Via Selective Laser Melting, International Journal of Fatigue. (2019) 13.
- [37] D. Qi, H. Yu, M. Liu, H. Huang, S. Xu, Y. Xia, G. Qian, W. Wu, Mechanical behaviors of SLM additive manufactured octet-truss and truncated-octahedron lattice structures with uniform and taper beams, International Journal of Mechanical Sciences. 163 (2019) 105091. https://doi.org/10.1016/j.ijmecsci.2019.105091.
- [38] J.L. Gonzalez-Velazquez, Fractography and failure analysis, Springer Berlin Heidelberg, New York, NY, 2018.
- [39] W. Radlof, C. Benz, M. Sander, Numerical and experimental investigations of additively manufactured lattice structures under quasi-static compression loading, Material Design & Processing Communications. n/a (2020) e164. https://doi.org/10.1002/mdp2.164.
- [40] X. Cao, Y. Jiang, T. Zhao, P. Wang, Y. Wang, Z. Chen, Y. Li, D. Xiao, D. Fang, Compression experiment and numerical evaluation on mechanical responses of the lattice structures with stochastic geometric defects originated from additive-manufacturing, Composites Part B: Engineering. 194 (2020) 108030. https://doi.org/10.1016/j.compositesb.2020.108030.
- [41] A. El Elmi, D. Melancon, M. Asgari, L. Liu, D. Pasini, Experimental and numerical investigation of selective laser melting—induced defects in Ti–6Al–4V octet truss lattice material: the role of material microstructure and morphological variations, Journal of Materials Research. (2020) 1–13. https://doi.org/10.1557/jmr.2020.75.
- [42] M. Mazur, M. Leary, S. Sun, M. Vcelka, D. Shidid, M. Brandt, Deformation and Failure Behaviour of Ti-6Al-4V Lattice Structures Manufactured by Selective Laser Melting (SLM), The International Journal of Advanced Manufacturing Technology. 84 (2016) 1391–1411. https://doi.org/10.1007/s00170-015-7655-4.
- [43] A.B. Arshad, A. Nazir, J.-Y. Jeng, The effect of fillets and crossbars on mechanical properties of lattice structures fabricated using additive manufacturing, The International Journal of Advanced Manufacturing Technology. 111 (2020) 931–943. https://doi.org/10.1007/s00170-020-06034-x.
- [44] L.J. Gibson, M.F. Ashby, Cellular solids: structure and properties, 1997. http://dx.doi.org/10.1017/CBO9781139878326 (accessed June 9, 2020).